Magnetic properties of tetragonal $SmFe_{12-x}Mo_x$ in bulk and melt-spun ribbons

B. Rodríguez-Crespo, A. Garcia, J. Rosero, C. Echevarria-Bonet, J.M. Porro, D. Salazar

---

B. Rodríguez-Crespo, A. Garcia, J. Rosero, J.M. Porro, D. Salazar

BCMaterials, Basque Center Centre for Materials, Applications and Nanostructures, UPV/EHU Science Park, 48940 Leioa, Spain

E-mail: daniel.salazar@bcmaterials.net

C. Echevarria-Bonet

Department of Physics, University of Oviedo, 33007 Oviedo, Spain,

J.M. Porro

IKERBASQUE, Basque Foundation for Science, Plaza Euskadi 5, 48009 Bilbao, Spain

---

Abstract

Currently, electric motors and generators use high energy permanent magnets based on $RE_2Fe_{14}B$ phases (RE: rare earth) with high amounts of RE often including heavy-RE metals (Dy, Tb), the most critical group of the raw materials. $REFe_{12}$ alloys are seen as potential alternatives to RE2Fe14B since they have a significantly lower amount of RE-metals with similar or better values of remnant magnetization (MR) and high magnetocrystalline anisotropy (MCA), which can give rise to a large energy product (BH)max [1]. In this work we study the ribbons of $SmFe_{12-x}Mo_x$ (x=0.5, 1) alloys with wheel speeds of $15 m \cdot s^{-1}$ and $35 m \cdot s^{-1}$ and the effect of heat treatments on the coercivity and magnetic properties. Maximum coercivity after heat treatments was obtained in ribbons that were as-spun at $35 m \cdot s^{-1}$. For x=0.5, $\mu_0 H_c$ increases from 0.06 T to 0.36 T and for x=1.0 the coercivity was enhanced from 0.02 T to 0.34 T. The highest values of saturation magnetization were obtained in ribbons with composition x=0.5 (~$145 A \cdot m^2 kg^{-1}$).

1. Introduction

Fast emerging green technologies demand the use of high power permanent magnets as the main part of electric motors and generators for energy production[1], hybrid and electric cars[2], aviation[3], etc. These permanent magnets are based on RE rich alloys (RE: rare earth), mainly with $RE_2Fe_{14}B$ phases[4] including heavy-RE metals (Dy, Tb), one of the most critical group of the raw materials[5]. The environmental impact of RE extraction[6,7] and their large price fluctuation over recent years[8] has led to find solutions that use less RE based permanent magnets. $REFe_{12}$ alloys are seen as potential alternatives to conventional $RE_2Fe_{14}B$ ones since they have a significantly lower amount of RE-metals (around 7.7% against 12% of the latter) with similar or better values of remnant magnetization (M_R) and high magnetocrystalline anisotropy (MCA), which can give rise to a large energy product $(BH)_{max}$.[9]

Regarding the 1:12 phases, this family of alloys is very interesting for permanent magnet applications due to their high values of saturation magnetization, anisotropy field and Curie temperature. However, the RFe_{12} compound needs the addition of a transition metal (M) (i.e. Ti, Si, Mo) replacing Fe in order to stabilize the $ThMn_{12}$ tetragonal structure that gives rise to the high values of MCA. Several experimental works.[10,11] combined with theoretical predictions of $ThMn_{12}$-type phases[12] give a useful summary of the current state of this topic. Around this $RFe_{12-x}M$ compounds several studies have been already performed. A. Hütten et al. studied the system of $SmFe_{10}Ti$ containing two phases; the α – Fe phase and $SmFe_{11}Ti$ phase, with the 1:12 structure.[13] They found a temperature dependence of the coercivity analysed in terms of pinning (at high temperatures) and nucleation mechanisms (at lower temperatures). Similarly, phase relations in the Sm-Fe-V system were studied by S. Sugimoto et al. and they found various phases to be present for $Sm_3(Fe,V)_{29}$ compound. The Sm-Fe-Co compound was studied by H. Sepehri-Amin et al. and they reported a coercivity of 1.2 T with a high remanent magnetization of 1.5 T.[14] Other studies performed by S. Khazzan et al. analysed the nanostructured Sm-Fe-Mo magnetic material that exhibited enhanced magnetic properties.[15] They concluded that the effect of annealing temperature on the coercivity makes this alloy suitable for permanent magnets.

Thus, in this work we study the system $SmFe_{12}$ with small substitutions of Mo in order to stabilize the 1:12 tetragonal structure and determine its effect on the MCA and the resulting coercivity in nanostructured magnets. For this aim, a set of $SmFe_{12-x}Mo_x$ (x=0.5, 1) ribbons as-spun at wheel-speeds of $15 m \cdot s^{-1}$ and $35 m \cdot s^{-1}$ are studied and compared. The effect of thermal treatments is studied for the melt-spun ribbons in order to get highest coercivity and energy product $(BH)_{max}$.

2. Experimental methods

Alloys with nominal compositions $SmFe_{12-x}Mo_x$ (x = 0.5, 1) were arc-melted from pure constituents and then annealed at 1050 ºC for 48 h. An excess of 10 wt.% of Sm was added in order to consider the Sm losses due to some evaporation during melting, so that the 1:12 phase would be eventually obtained. These alloys were used to study the intrinsic properties of the 1:12 phase on field-oriented powders. Subsequently, extrinsic properties were studied in melt-spun ribbons; the alloys were melt-spun at two wheel-speeds of 15 and 35 $m \cdot s^{-1}$, into amorphous or highly disordered ribbons. The

ribbons were heat-treated in vacuum at different temperatures ranging from 650 ºC to 950 ºC for different times between 3 and 40 min in order to obtain nanostructured ribbons that crystallized in the $ThMn_{12}$ tetragonal structure. Structural characterization of the samples was carried out by X-ray diffraction (XRD) using Cu-Kα radiation on random and oriented powders, using the Bragg-Brentano geometry, at room temperature (RT). XRD patterns were analysed by Rietveld refinements through the FullProf Suite,[16] using a Thompson-Cox-Hastings pseudo-Voigt function to describe the profile of the peaks. The microstructural characterization and direct determination of the composition of the samples was done by EDS in a scanning electron microscopy (SEM, JEOL JSM-6400). RT and temperature dependant magnetic measurements were performed with Quantum Design PPMS magnetometer and MicroSense EZ7 vibrating sample magnetometer (VSM). Powders analysed were hand-milled and oriented under magnetic field (1.85 T) in an epoxy matrix when necessary.

RT Mössbauer spectroscopy (MS) was carried out at RT in the transmission geometry using a conventional constant-acceleration spectrometer with a ^{57}Co-Rh source. The NORMOS (1990) software package developed by R. A. Brand[17] was used to fit these spectra.

3. **Results and analysis**

3.1. Bulk alloys

The intrinsic properties of SmFeMo give information about the stability of the 1:12 uniaxial structure with respect to the addition of Mo. For both compositions, we can observe a full stabilization of the tetragonal phase and values of saturation magnetization and anisotropy field promising for permanent magnet applications.

3.1.1 Structural analysis

X-ray diffraction patterns for samples in bulk after long heat treatment of 1050 ºC for 48h are shown in Figure 1. Diffraction peaks observed in this figure, identified by Rietveld refinement (see Figure S1 of Supplementary Material); mainly correspond to the $ThMn_{12}$-type tetragonal structure and to a small amount of a secondary phase, the bcc α-Fe. The amount of this secondary phase, estimated by Rietveld as around 20 wt.% for both samples, and the lattice parameters are summarized in the Table 1. For x = 1, the unit cell volume is 350.1 $Å^3$ and the c/a ratio is 0.5588, while for x = 0.5 the volume contracts to 348.3 $Å^3$ and c/a = 0.5587. Although c/a is slightly lower for x = 0.5, the effect of the composition on the cell volume is more evident and could result in the enhancement of the intrinsic properties. To determine these magnetic properties, powdered samples were oriented by an external magnetic field along the easy magnetization-axis (c-lattice). XRD patterns of the oriented samples shows in the inset of figure 1 a single peak (0 0 2) corresponding to the diffraction plane perpendicular to the c-axis, allowing to ensure a well-oriented sample for the evaluation of the intrinsic magnetic properties.

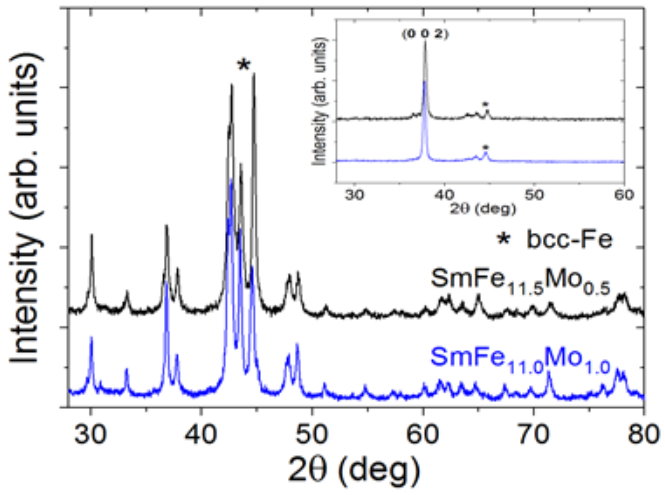

Figure 1. X-ray diffraction patterns of $SmFe_{12-x}Mo_x$ bulk samples after long heat treatments. (inset) XRD patterns of oriented powdered samples.

Table 1. Summary of parameters obtained after Rietveld refinement of samples with long heat treatment.

		1: 12 phase				bcc-Fe phase	
Compound	Real composition (by XRD)	x - 8j	x - 8i	a (Å)	c (Å)	a (Å)	weight %
$SmFe_{11.0}Mo_{1.0}$	$Sm_{1.011}Fe_{11.0}Mo_{0.993}$	0.2795(5)	0.3556(5)	8.5570(2)	4.7819(1)	2.8838(1)	19.7(9)
$SmFe_{11.5}Mo_{0.5}$	$Sm_{0.975}Fe_{11.5}Mo_{0.489}$	0.2767(5)	0.3594(5)	8.5422(2)	4.7733(2)	2.8761(1)	21.9(3)

3.1.2 Intrinsic magnetic properties

Magnetization curves for the two (bulk) samples with the magnetic field applied in the parallel and perpendicular directions to the easy-magnetization axis are shown in Figure 2. Two magnetic features are distinguished as an effect of the Mo reduction; as expected, the saturation magnetization of the sample with less Mo content is higher due to the higher amount of Fe. Moreover, the anisotropy field increases for the lower Mo content. A summary of these values is included in the Table 2.

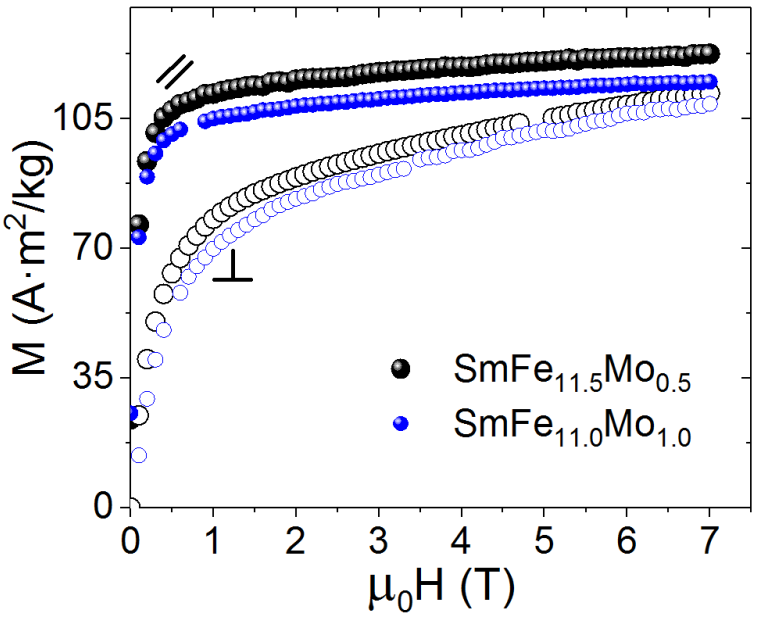

Figure 2. Magnetization curves of the oriented $SmFe_{12-x}Mo_x$ (x=0.5 and 1) powders, which were measured with the magnetic field applied in parallel (//) and perpendicular (⊥) to the easy axis.

Values of saturation magnetization and anisotropy field are obtained by the Law of Approach to Saturation and by a linear extrapolation of perpendicular and parallel M(H) curves at high fields, respectively (see Figure S4). As commented, saturation magnetization increases up to 123 $A \cdot m^2 kg^{-1}$ for x=0.5, and the anisotropy field reaches 11 T, while for x = 1; M_S = 115 $A \cdot m^2 kg^{-1}$ and $\mu_0 H_a$ = 8T. The obtained values on our samples are comparable to those reported by Kou et al. (10 and 7 T for x = 0.5 and 1, respectively) [18].

3.2. Melt-spun ribbons

3.2.1. On the search of the best heat treatment

Once the intrinsic properties are determined, we proceed to fabricate melt-spun ribbons to develop coercivity in these alloys. First, the effect of the wheel-speed on the thickness of as-spun ribbons was studied through SEM images for the two wheel-speeds used in this work (see Figure 3).

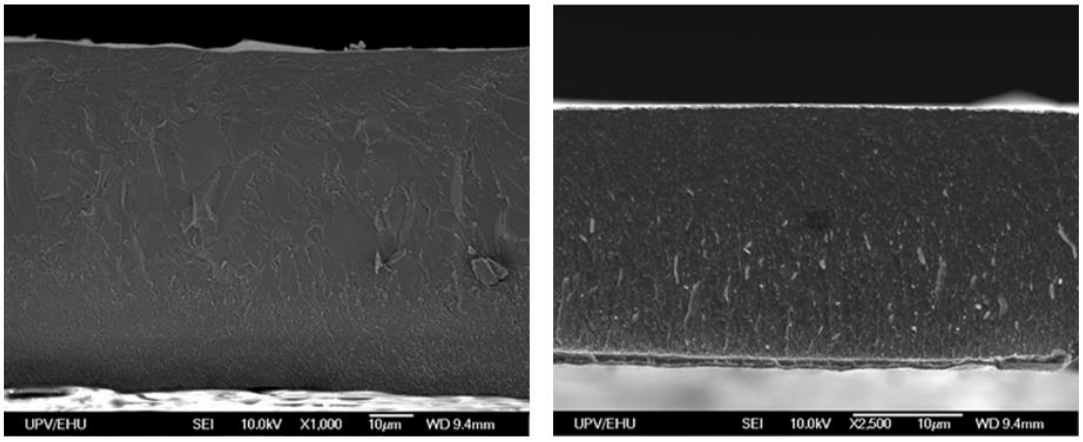

Figure 3: SEM images of as-spun ribbons at wheel speeds of 15 m·s^{-1} (left) and 35 m·s^{-1} (right). The thickness of the ribbons is 20 μm for 35 m·s^{-1} and 40-50 μm for 15 m·s^{-1}.

A small amount of bcc-Fe was present, due to the evaporation of Sm caused by the long annealing times after arc melting.[19] In the case of ribbons, the Sm loss was not that significant during heat treatments. This can be observed in the XRD patterns presented in Figure 4 where the effect of heat treatment is exhibited for $SmFe_{11.5}Mo_{0.5}$ spun at 15 m·s^{-1} and compared with the diffraction peaks corresponding with the $ThMn_{12}$ -type phase.

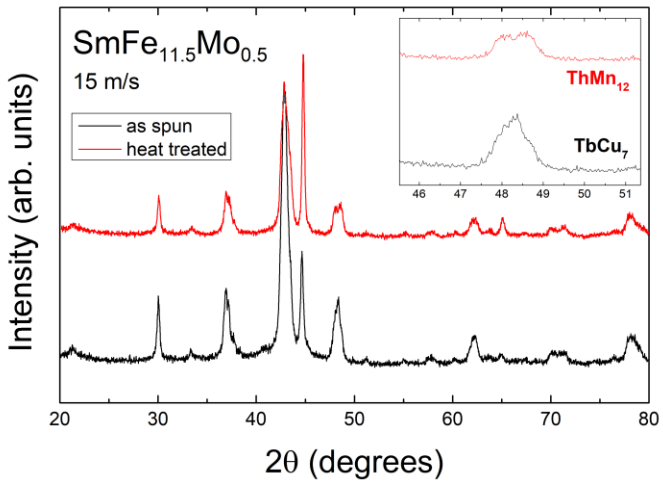

Figure 4: Effect of heat treatment for $SmFe_{11.5}Mo_{0.5}$ at 15 m·s^{-1} and comparation with $ThMn_{12}$ and $TbCu_7$ (inset).

XRD patterns for melt-spun ribbons (left) and the effect of the optimized heat treatments for the treated ribbons (right) is shown in Figure 5, and it is evidence that there is no notable increase in bcc-Fe content but an improvement in the crystallization of the 1:12 phase.

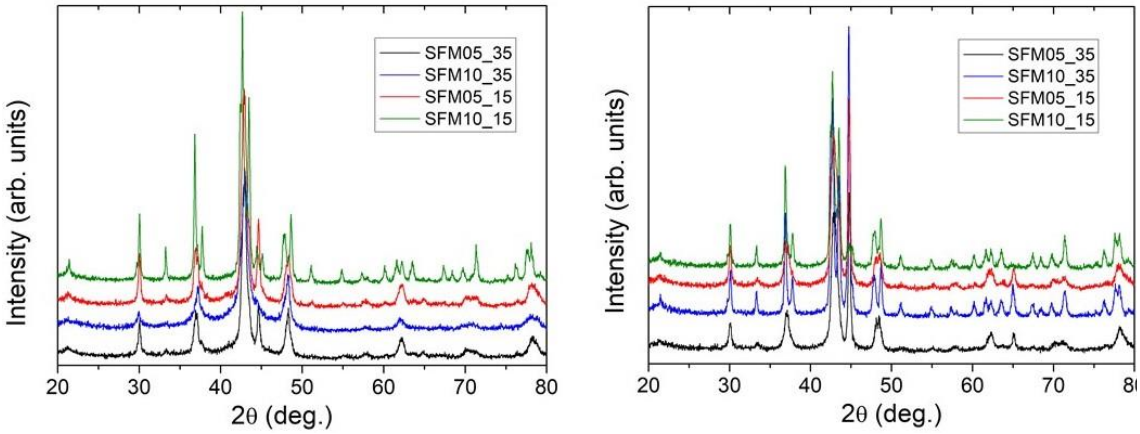

Figure 5: XRD of the melt-spun (left) and heat treated (right) ribbons, after an optimized heat treatment for each sample

The evolution of the coercivity and remnant magnetization as a function of the temperature and heat treatment duration was studied and compared for each sample (see Figure 6 and Supplementary material). The optimal heat treatment for each sample is summarized in Table 2.

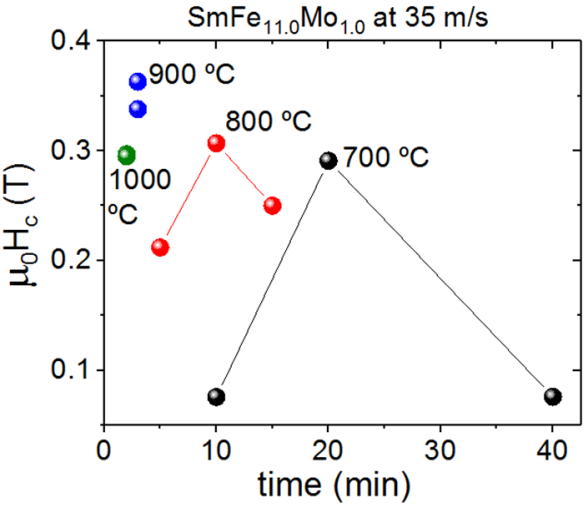

Figure 6: Evolution of coercivity as a function of heat treatment for $SmFe_{11.0}Mo$ at 35 $m{\cdot}s^{-1}$.

For the $SmFe_{11.5}Mo_{0.5}$ ribbons, we can compare the demagnetization curves in Figure 7, for different wheel-speeds during melt spinning. We can see that there is no much difference in the magnetization and coercivity values for the crystallized ribbons, though in the case of the ribbons produced with a wheel-speed of 35 $m \cdot s^{-1}$, the magnetization is a bit higher than for 15 $m \cdot s^{-1}$. These values are presented in Table 2, together with the remnant magnetization. Also, the saturation magnetization shows a significate increase (~144 $Am^2 \cdot kg^{-1}$) for ribbons with x=0.5.

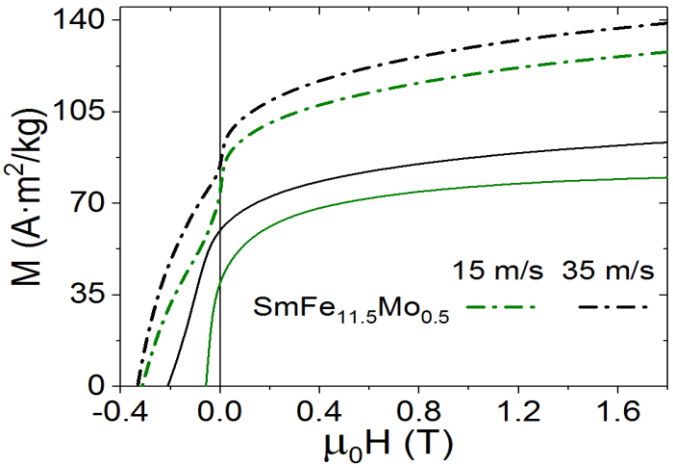

Figure 7: Demagnetization curves of as-spun (solid lines) and crystallized (dotted lines) of the $SmFe_{11.5}Mo_{0.5}$ ribbons, produced with two wheel-speeds during melt spinning.

3.2.2. Structural analysis of the annealed ribbons

The structural analysis of the ribbons exhibiting the highest coercivity was carried out by Rietveld refinement of the XRD patterns (see Figure 8.) for the estimation of the composition, lattice parameter, crystallite size and phase concentration of the 1:12 and the bcc-Fe phases evidenced in the patterns. A summary of the lattice parameters and crystallographic data obtained by Rietveld analysis is listed in Table 2. These results estimate a slight drop in Sm concentration from 1.0 to 0.97 and 0.94 for samples with x = 0.5 and 1.0, respectively, indicating a possible evaporation of Sm during heating process. Lattice parameters keep constant with wheel speed but a contraction in *a-lattice* and expansion in *c-lattice* parameter is observed for the 1:12 phase when Mo is reduced to 0.5. Additionally, c/a ratio increases from 0.560 to 0.567 by Mo reduction. However, *a-lattice* parameter of the bcc phase keeps constant. The grain size of the 1:12 phase is about 80 nm and 45 nm for the bcc-Fe phase. The concentration of bcc-Fe phase determined by Rietveld refinement varies between 6 and 33%.

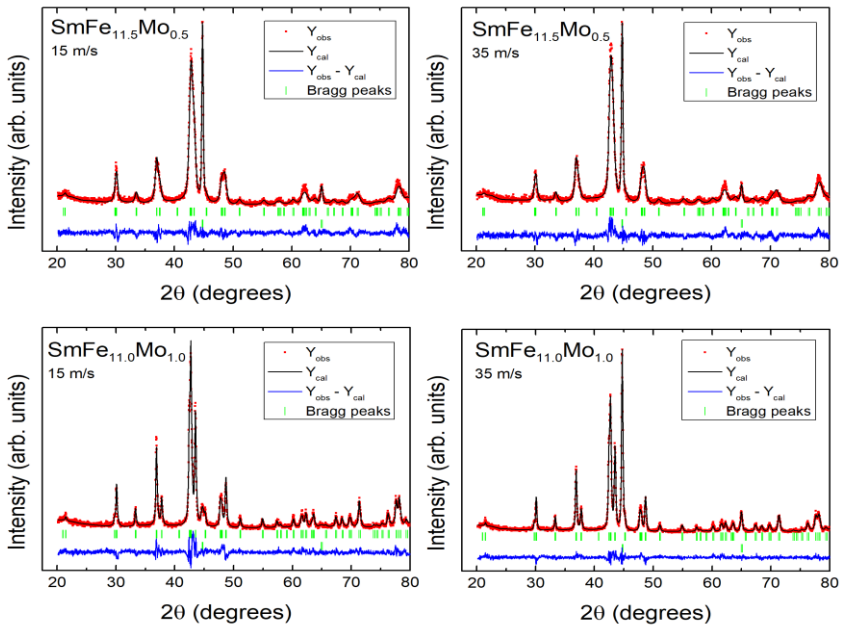

Figure 8: Rietveld refinements of the XRD patterns on melt-spun ribbons with optimal heat treatment (see heat treatments in Table 2).

Table 2: Crystallographic data of the two studied compounds (x = 0.5 and 1), produced by two wheel-speeds by melt spinning (15 and 35 m·s^{-1}), and annealed with the best heat treatment. These values were obtained after Rietveld refinements of the XRD patterns; x – 8j and x – 8i correspond to the atomic position x of the 8j and 8i atomic sites, a and c to the lattice parameters and D is the particle size. The weight percentage of the bcc-Fe phase is also provided. Least significant number error in parentheses.

				1:12 phase					bcc-Fe phase		
Compound	Wheel speed (m·s^{-1})	Best HT: T (ºC) – t (min)	Real composition (by XRD)	x - 8j	x - 8i	a (Å)	c (Å)	D (nm)	a (Å)	D (nm)	weight %
$SmFe_{11.0}Mo_{1.0}$	15	700 - 10	$Sm_{0.966}Fe_{11.0}Mo_{0.999}$	0.2809(5)	0.3558(5)	8.5525(2)	4.7901(2)	84(1)	2.8800(4)	38(1)	6.1(3)
$SmFe_{11.0}Mo_{1.0}$	35	900 - 3	$Sm_{0.976}Fe_{11.0}Mo_{0.999}$	0.2811(4)	0.3565(4)	8.5512(1)	4.7909(1)	81(1)	2.8772(1)	41(1)	33.1(3)
$SmFe_{11.5}Mo_{0.5}$	15	900 - 5	$Sm_{0.941}Fe_{11.0}Mo_{0.503}$	0.2773(6)	0.3574(6)	8.5014(4)	4.8185(4)	76(1)	2.8726(1)	50(1)	22.6(4)
$SmFe_{11.5}Mo_{0.5}$	35	900 - 5	$Sm_{0.907}Fe_{11.0}Mo_{0.500}$	0.2802(4)	0.3578(6)	8.4966(4)	4.8311(4)	77(1)	2.8737(1)	44(1)	25.1(4)

3.2.3. Mössbauer spectroscopy

Figure 9.a. shows the experimental RT Mössbauer spectrum of the $SmFe_{11.5}Mo_{0.5}$ (black) and $SmFe_{11.0}Mo_{1.0}$ (blue) crystallized ribbons, produced at 35m·s^{-1}. The site assignment of the hyperfine parameters was ruled by the correlation between the isomer shift δ and the Wigner–Seitz cell volume (WSV), calculated using crystallographic data derived from Rietveld refinements. As pointed in the

figure, a second Fe-based phase was found in the two spectra, which corresponds with bcc-Fe, confirming Rietveld refinements of the XRD data. SEM images of the as-spun $SmFe_{11.5}Mo_{0.5}$ ribbons, spun at 15 (up) and 35 $m \cdot s^{-1}$ (down), are shown in Figure 9.b. Apart from the Sm-Fe-Mo grains (around 200nm in size, see Table 3), a secondary phase is clearly detected as white spots, corresponding to Sm nanograins (<45nm). The presence of these nanoprecipitations of Sm correlates with the evaporation of Sm that occurs during heat treatments.

Table 3: Grain size and Sm-rich phase size for each sample.

Sample	$SmFe_{11.5}Mo_{0.5}$ 15m·s^{-1}	$SmFe_{11.5}Mo_{0.5}$ 35m·s^{-1}	$SmFe_{11}Mo$ 15m·s^{-1}	$SmFe_{11}Mo$ 35m·s^{-1}
Average grain diameter (nm)	376 ± 102	280 ± 50	215 ± 80	133 ± 30
Samarium diameter (nm)	44 ± 9	40 ± 9	N/A	N/A

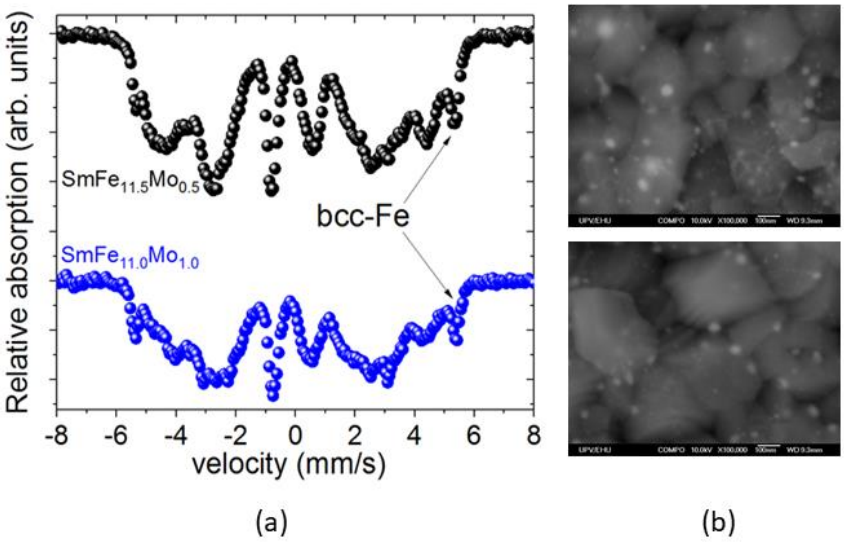

Figure 9: Characterization of ribbons with optimal heat treatment (a) Mössbauer spectra of SmFe11.5Mo0.5 at 35 m·s^{-1} and (b) SEM images of samples SmFe11.5Mo0.5 as-spun (above) at 15 and (below) 35 m·s^{-1}. Both experiments show secondary phases contributions; Mössbauer detects the bcc-Fe and Sm-rich phase is observed in SEM as brightest spots.

3.2.4. Extrinsic magnetic properties

A summary of the magnetic properties of the heat-treated ribbons melt-spun at two-wheel speeds (15 and 35 $m \cdot s^{-1}$) is presented in Table 4. The sample with the lowest Mo content, showing the highest anisotropy field (11 T), exhibits better properties when spun at 15 $m \cdot s^{-1}$ but, after heat treatment, is the sample as-spun at 35 $m \cdot s^{-1}$ the one that shows the highest coercivity and saturation magnetization reported in this work, 0.36 T and 145 $A \cdot m^2 kg^{-1}$, respectively. A similar behavior was observed for the alloys with x=1.0, ribbons spun at a lower wheel speed shows better properties than those obtained

at 35 $m \cdot s^{-1}$, however, it is the latter that shows higher coercivity and saturation magnetization after heat-treatment. In general, these compounds showed high anisotropy field values but did not develop a coercivity consistent with the estimated H_a. Although a fine nanostructure was obtained for the heat-treated ribbons, the coercivity increases only up to 0.36T, possibly due to the formation of large amounts of the bcc-Fe secondary phase. Prior to the implementation of these alloys in permanent magnet technology, a better microstructure must be defined to prevent loss of Sm by evaporation during processing.

Table 4: Magnetic properties of SmFe12-xMox bulk and as spun and crystallized melt-spun ribbons (with the best heat treatments, reported above).

	bulk	Wheel speed	as-spun			crystallized		
Mo (x)	H_a (T)	($m \cdot S^{-1}$)	M_S ($A \cdot m^2 kg^{-1}$)	M_R ($A \cdot m^2 kg^{-1}$)	$\mu_0 H_C$ (T)	M_S ($A \cdot m^2 kg^{-1}$)	M_R ($A \cdot m^2 kg^{-1}$)	$\mu_0 H_C$ (T)
0.5	11	15	98.5	59.9	0.21	144.7	64.0	0.33
0.5		35	81.7	39.7	0.06	145.7	61.2	0.36
1.0	8.5	15	79.1	44.3	0.17	82.5	50.3	0.24
1.0		35	83.1	43.1	0.02	87.3	49.9	0.34

4. Conclusion

In conclusion, low molybdenum substitutions (x=0.5) can stabilize the uniaxial 1:12 structure maintaining a high MCA, with anisotropy field values above 10T. The coercivity was developed for as-spun ribbons through heat treatments. The values of the coercivity after the optimal heat treatment (0.36 T) are still low with respect to Ha. This could be due to the crystallization of the Fe-bcc phase during the sample processing as a consequence of the samarium evaporation. Thus, the best stoichiometry and heat treatment for the highest magnetic properties is the $SmFe_{11.5}Mo_{0.5}$ spun at wheel speed of $35 m \cdot s^{-1}$ and at 850ºC. In summary, both intrinsic and extrinsic magnetic properties show that $SmFe_{11.5}Mo_{0.5}$ is a good candidate material for up-scaling. However, we would expect some problems due to Sm-evaporation during industrial techniques as strip casting, which should be avoided.

5. References

[1] Y. El Mourabit, A. Derouich, A. Allouhi, A. El Ghzizal, N. El Ouanjli, O. Zamzoumyes, *Int. Trans. Electr. Energy Syst.* **2020**, *30*, 1.

[2] C. Liu, K. T. Chau, J. Z. Jiang, *IEEE Trans. Ind. Electron.* **2010**, *57*, 4055.

[3] A. J. Mitcham, J. J. A. Cullen, **2002**.

[4] S. J. Collocott, J. B. Dunlop, H. C. Lovatt, V. S. Ramsden, *Mater. Sci. Forum* **1999**, *315–317*, 77.

[5] T. E. Graedel, E. M. Harper, N. T. Nassar, P. Nuss, B. K. Reck, **2015**, *112*, 4257.

[6] N. Haque, A. Hughes, S. Lim, C. Vernon, *Resources* **2014**, *3*, 614.

[7] J. M. D. Coey, *Engineering* **2020**, *6*, 119.

[8] H. Paulick, E. Machacek, *Resour. Policy* **2017**, *52*, 134.

[9] G. C. Hadjipanayis, A. M. Gabay, A. M. Schönhöbel, A. Martín-Cid, J. M. Barandiaran, D. Niarchos, *Engineering* **2020**, *6*, 141.

[10] A. M. Gabay, A. Martín-Cid, J. M. Barandiaran, D. Salazar, G. C. Hadjipanayis, *AIP Adv.* **2016**, *6*, DOI 10.1063/1.4944066.

[11] A. M. Gabay, G. C. Hadjipanayis, *Scr. Mater.* **2018**, *154*, 284.

[12] W. Körner, G. Krugel, C. Elsässer, *Sci. Rep.* **2016**, *6*, 1.

[13] A. Hütten, G. Thomas, *J. Appl. Phys.* **1991**, *70*, 6113.

[14] H. Sepehri-Amin, Y. Tamazawa, M. Kambayashi, G. Saito, Y. K. Takahashi, D. Ogawa, T. Ohkubo, S. Hirosawa, M. Doi, T. Shima, K. Hono, *Acta Mater.* **2020**, *194*, 337.

[15] S. Khazzan, L. Bessais, G. Van Tendeloo, N. Mliki, *J. Magn. Magn. Mater.* **2014**, *363*, 125.

[16] J. Rodríguez-carvajal, **2003**.

[17] R. A. Brand, J. Lauer, D. M. Herlach, *J. Phys. F Met. Phys.* **1983**, *13*, 675.

[18] X. C. Kou, E. H. C. P. Sinnecker, R. Grössinger, G. Wiesinger, T. Zhao, J. P. Liu, F. R. de Boer, *J. Magn. Magn. Mater.* **1995**, *140–144*, 1025.

[19] A. Martin-Cid, A. M. Gabay, D. Salazar, J. M. Barandiaran, G. C. Hadjipanayis, *Phys. Status Solidi Curr. Top. Solid State Phys.* **2016**, DOI 10.1002/pssc.201600102.